aerospace

MDPI

Article

# Impact of Solar Irradiance on Low-Earth-Orbit Satellite Orbital Decay During Geomagnetic Storm

**Haiquan Yu [1,2], Lue Chen [1,2,*] and Bo Chen [1,2,*]**

[1] School of Aerospace, Harbin Institute of Technology Shenzhen, Shenzhen 518055, China; 20s058089@stu.hit.edu.cn

[2] Key Laboratory of Aerospace RS Big-Data Intelligent Processing and Application of Guangdong Higher Education Institute, Harbin Institute of Technology Shenzhen, Shenzhen 518055, China

* Correspondence: chenlue@hit.edu.cn (L.C.); hitchenbo@hit.edu.cn (B.C.)

**Abstract**

In recent years, with the rapid expansion of low-Earth-orbit (LEO) satellite constellations, the orbital decay of LEO satellites caused by atmospheric heating from solar irradiance and geomagnetic activity has become increasingly prominent. Accurately understanding the orbital decay behavior of LEO satellites during geomagnetic storms is essential for managing orbital lifetime, orbit determination, orbit control, and collision risk assessment. This study investigates the combined effects of solar radiation intensity and geomagnetic storm intensity on LEO satellite orbital decay by analyzing 130 representative intense geomagnetic storms from 1965 to 2025. The results demonstrate that during geomagnetic storms, both solar irradiance and geomagnetic activity jointly influence orbital decay: solar irradiance primarily determines the total decay magnitude, while geomagnetic activity mainly affects short-term decay rates through transient disturbances. Furthermore, solar radiation intensity shows a stronger correlation with orbital decay than storm intensity. Therefore, effective orbit maintenance strategies for LEO satellites should emphasize the influence of solar radiation intensity in addition to geomagnetic storm intensity. Our findings provide valuable references for developing operational orbit maintenance protocols for LEO satellites during space weather events.

**Keywords:** orbital decay; solar irradiance; geomagnetic activity; LEO satellites; thermospheric density



Academic Editor: Paolo Tortora

Received: 27 October 2025

Revised: 25 November 2025

Accepted: 3 December 2025

Published: 4 December 2025

**Citation:** Yu, H.; Chen, L.; Chen, B. Impact of Solar Irradiance on Low-Earth-Orbit Satellite Orbital Decay During Geomagnetic Storm. *Aerospace* **2025**, *12*, 1084. https://doi.org/10.3390/aerospace12121084



## 1. Introduction

In recent years, with the rapid advancement of space technology and increasing frequency of space activities, low-Earth-orbit (LEO) operations—centered around LEO satellites—have become a major focus of global space development. Compared with traditional medium- and high-altitude-orbit satellites, LEO satellites offer significant advantages, including lower launch costs, reduced communication latency, broader coverage, enhanced observational capability, and improved system redundancy. These unique strengths in communication, remote sensing, and navigation domains have underscored their considerable commercial and military value. Inspired by mega-constellations such as Starlink and OneWeb, countries worldwide are actively developing LEO satellites and even competing for strategic orbital resources. However, the very feature that enables these advantages—their lower orbital altitude—also renders LEO satellites more susceptible to atmospheric drag and more sensitive to variations in the space environment. This heightened sensitivity directly impacts orbit determination accuracy, collision probability assessment, orbital lifetime, and ultimately, the successful execution of satellite missions and functionality.

Atmospheric drag stands as the dominant non-conservative force and primary cause of orbital decay for low-Earth-orbit (LEO) satellites. The magnitude of this drag is determined largely by thermospheric density, which in turn is strongly influenced by solar-driven space weather. Variations in geomagnetic activity and solar irradiance can significantly alter thermospheric density. If a LEO spacecraft fails to respond promptly and appropriately to such drag effects caused by space weather, severe consequences may ensue, as illustrated by the following historical cases:

- In 1979, increased solar activity caused upper atmospheric expansion and a corresponding rise in thermospheric density, leading to the premature reentry of the Skylab space station [1].
- In 2001, heightened solar activity resulted in the Mir space station decaying at an average rate of approximately 1.5 km per day due to enhanced atmospheric drag—a major contributor to its eventual controlled deorbit [2].
- In February 2022, a geomagnetic storm led to increased atmospheric density, causing 40 out of 49 newly launched Starlink satellites to fail to reach orbit and burn up in the atmosphere, representing a significant economic loss [3].

Beyond these direct impacts, variations in atmospheric drag also complicate the identification and tracking of satellites and space debris, and hinder accurate predictions of satellite lifetime and collision probability. Therefore, investigating the orbital decay behavior of LEO satellites during geomagnetic storms is essential for improving precise orbit determination, generating effective avoidance strategies, and conducting reliable collision risk assessments.

The primary energy source driving variations in thermospheric density is solar radiation, particularly soft X-ray and extreme ultraviolet (EUV) emissions, which exert long-term influences on the thermosphere. Consequently, solar radiation plays a decisive role in shaping the basic structural distribution and periodic variations of thermospheric density [4]. On longer time scales, thermospheric density exhibits a strong correlation with the solar activity cycle. Classified by sunspot number, solar activity follows an approximately 11-year cycle, to which variations in thermospheric density closely correspond [5–7]. Emmert [8] analyzed thermospheric mass density trends derived from satellite orbital data between 1967 and 2005, reporting a decline of 2.0 $\pm$ 0.5% per decade at an altitude of 400 km during this period. Additionally, due to solar rotation, observed solar irradiance at Earth exhibits a periodic variation of approximately 27 days, on which timescale thermospheric density also fluctuates in response to changes in solar radiation intensity [9–11]. Furthermore, Le et al. [12] investigated changes in thermospheric density during solar flares using atmospheric density data measured by the CHAMP and GRACE satellites, while Huang et al. [13] coupled the Flare Irradiance Spectral Model (FISM) with the Thermosphere–Ionosphere-Electrodynamics General Circulation Model (TIE-GCM) to examine the impact of solar flares on multi-band electromagnetic radiation and thermospheric density. Both studies consistently demonstrated a high correlation between solar flares and enhanced thermospheric density.

Geomagnetic activity is the dominant factor causing short-term, rapid changes in thermospheric density. During geomagnetic storms, the Earth’s magnetosphere undergoes intense driving, leading to substantial energy and momentum injection into the high-latitude ionosphere–thermosphere system via field-aligned currents [14]. This energy input enhances ion motion, which in turn increases collisions between ions and neutral particles in the ionosphere. As a result, neutral particles are heated through collisions, ionization, and chemical reactions, and subsequently move upward into higher regions of the thermosphere. This process heats the high-latitude thermosphere and increases its density. Large-scale gravity wave-driven global wind surges then develop at high latitudes and transport energy toward middle and low latitudes through convection—a phenomenon known as Traveling Atmospheric Disturbances (TADs). TADs play a critical role in redistributing energy within the thermosphere [15]. Using Superposed Epoch Analysis (SEA), Oliveira et al. [16] investigated thermospheric heating during coronal mass ejection (CME)-driven magnetic storms, showing that heating energy propagates from high latitudes to equatorial regions via TADs within 3 hours after the storm's main phase onset.

Kim et al. [17] analyzed orbital variations of the KOMSAT-1 satellite between October and December 2003, concluding that short-term drag variations are primarily influenced by geomagnetic activity when the magnetosphere is disturbed by solar wind changes. Oliveira et al. [18] examined the effects of CME-induced geomagnetic storms on satellite orbits using data from the CHAMP and GRACE missions, finding that multiple CME-driven storms have more severe orbital impacts. Chen et al. [19] studied the influence of Corotating Interaction Regions (CIRs) on thermospheric density and satellite orbits, showing that while CME-induced storms cause brief but intense orbital decay, CIR-driven storms have a weaker but more prolonged effect. Reference [20] combined space weather parameters from four historically extreme geomagnetic storms (Dst $< -400$ nT) with orbital data from CHAMP and GRACE, using empirical atmospheric models to calculate density changes and assess drag effects during these events. Similarly, several researchers have analyzed SWARM satellite orbital data to study atmospheric drag effects on orbital decay during space weather events [21,22].

Regarding the recent large-scale reentry of Starlink satellites, Oliveira et al. [23,24] tracked and analyzed their reentry during Solar Cycle 25, demonstrating that geomagnetic storms influence the reentry speed and time taken to reach the Kármán line. For the Starlink loss event, researchers combined observational, forecast, and numerical simulation data to analyze the process, concluding that the loss was caused by a combination of space weather conditions, low orbital insertion, and increased area-to-mass ratio due to attitude changes [25,26].

Over the years, numerous scholars have made significant contributions to analyzing the effects of space weather events on satellite drag. However, on one hand, existing research has primarily focused on the influence of geomagnetic storm intensity on orbital decay rates, with relatively less attention paid to the effect of solar irradiance during storms. On the other hand, most studies have analyzed satellite orbital decay effects based on individual or a few specific geomagnetic storm events, resulting in limited sample sizes and localized analytical findings. To address these issues, this work presents the first large-scale analysis of LEO satellite orbital decay across geomagnetic storms of varying intensities. We selected 130 historically representative intense storm events to systematically examine the influence patterns of solar irradiance intensity and geomagnetic storm intensity on LEO satellite orbital decay. The analytical results demonstrate that solar radiation intensity is the dominant factor affecting LEO satellite orbital decay during geomagnetic storms. This conclusion can provide valuable references for developing orbit control strategies for LEO satellites during geomagnetic storms. The paper is structured as follows: Section 2 introduces the simulation analysis methods and models. Section 3 presents and discusses the experimental results. Section 4 provides the conclusion of this study.

## 2. Materials and Methods

Thermospheric density is strongly modulated by solar radiation and geomagnetic activity, which in turn governs the orbital decay of low-Earth-orbit (LEO) satellites through solar-driven space weather processes, as illustrated in Figure 1. A solar eruption enhances electromagnetic radiation across all bands; the thermosphere absorbs increased soft X-ray and extreme ultraviolet (EUV) radiation, leading to heating and a rise in atmospheric density that elevates aerodynamic drag on LEO satellites and accelerates orbital decay. Concurrently, coronal mass ejections (CMEs) release plasma and magnetic fields that interact with Earth's magnetosphere. When the interplanetary magnetic field is southward, magnetic reconnection with Earth's northward field triggers geomagnetic storms and substorms. This injects energetic particles into high-latitude regions via field-aligned currents, heating the upper atmosphere. The energy is then transported globally through convection and traveling atmospheric disturbances (TADs), causing worldwide thermospheric density perturbations. These variations further modify atmospheric drag on LEO satellites, resulting in additional orbital decay.

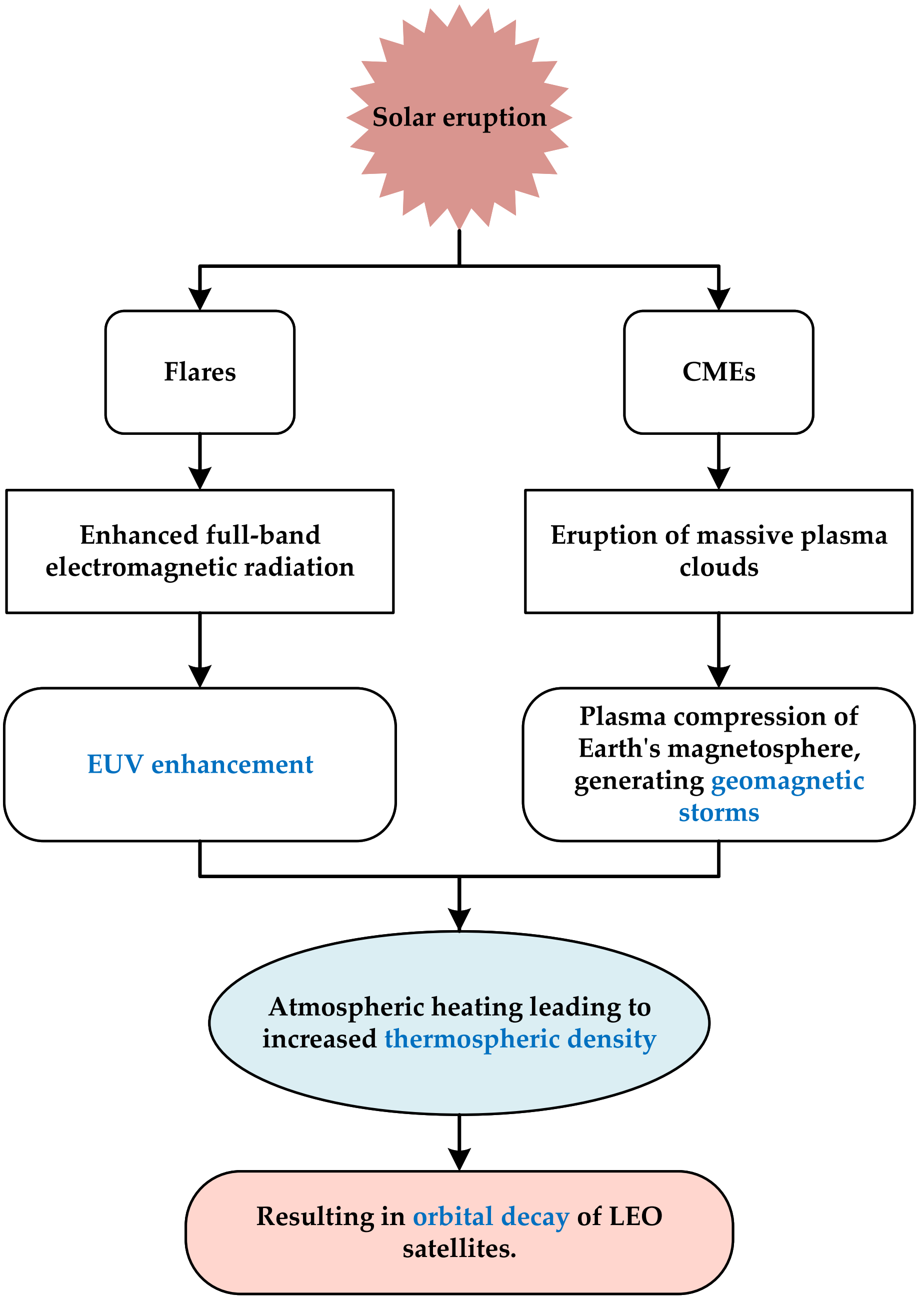


**Figure 1.** Fundamental Process of Solar Activity Impact on LEO Satellite Orbital Decay.

## *2.1. Solar Activity*

Solar activity intensity is commonly quantified using the F10.7 index, which measures the solar radio flux at a wavelength of 10.7 cm [27]. This index represents the solar flux density within a 100 MHz bandwidth centered at 2800 MHz (corresponding to a wavelength of 10.7 cm), with measurements typically reported hourly. The F10.7 index is expressed in solar flux units (sfu), where 1 sfu = $10^{-22}\ \mathrm{W} \cdot \mathrm{m}^{-2} \cdot \mathrm{Hz}^{-1}$. As a key indicator of solar activity, the F10.7 index exhibits a strong correlation with solar soft X-ray and extreme ultraviolet (EUV) radiation [28]. These spectral bands are significant drivers of thermospheric density variations [7]. Consequently, the F10.7 index serves as a primary input parameter for numerous thermospheric neutral density models and is widely employed in estimating thermospheric density and the associated satellite atmospheric drag. Solar activity levels are classified by various standards:

- The Australian Space Weather Forecast Centre utilizes sunspot number (SSN) to define six levels (Table 1).
- Chinese meteorological standards classify activity levels based on F10.7 index ranges (Table 2).

**Table 1.** Definition of solar activity level by SSN.

| Solar Activity Intensity | SSN |
|---|---|
| Extreme | >250 |
| Very High | 150–250 |
| High | 80–150 |
| Moderate | 40–80 |
| low | 20–40 |
| very low | 0–20 |

**Table 2.** Definition of solar activity level by F10.7 index .

| Solar Activity Intensity | F10.7 (sfu) |
|---|---|
| Very High | >200 |
| High | 150–200 |
| Moderate | 100–150 |
| low | 80–100 |
| very low | <80 |

## *2.2. Geomagnetic Activity*

Geomagnetic activity is commonly quantified using the Kp, Ap, and Dst indices [29].

- The Kp index is a quasi-logarithmic, three-hour index derived from magnetometer measurements at 13 globally distributed geomagnetic observatories. It ranges from 0 to 9 and represents the average disturbance level in the horizontal components of the geomagnetic field.
- The Ap index is the daily average of the derived 'ap' indices, which are obtained through a standardized conversion from the Kp values.
- The Dst index (Disturbance Storm Time) is an hourly index calculated from data collected by four low-latitude observatories. It specifically characterizes the reduction in the horizontal component of the Earth's magnetic field near the magnetic equator and serves as a crucial indicator of geomagnetic storm intensity.

## *2.3. Dynamics Modeling of the Satellite Orbital Decay*

To investigate variations in atmospheric drag and orbital decay (including changes in semi-major axis, altitude, and decay rate) experienced by low-Earth-orbit (LEO) satellites under diverse space weather conditions (primarily solar radiation variations and geomagnetic activity), this study establishes a dynamical model of space weather impacts on satellite orbital decay. The model comprises three core components: orbital perturbation calculation, atmospheric density computation, and numerical orbit propagation. The numerical simulation process for LEO satellite orbital decay is illustrated in Figure 2.

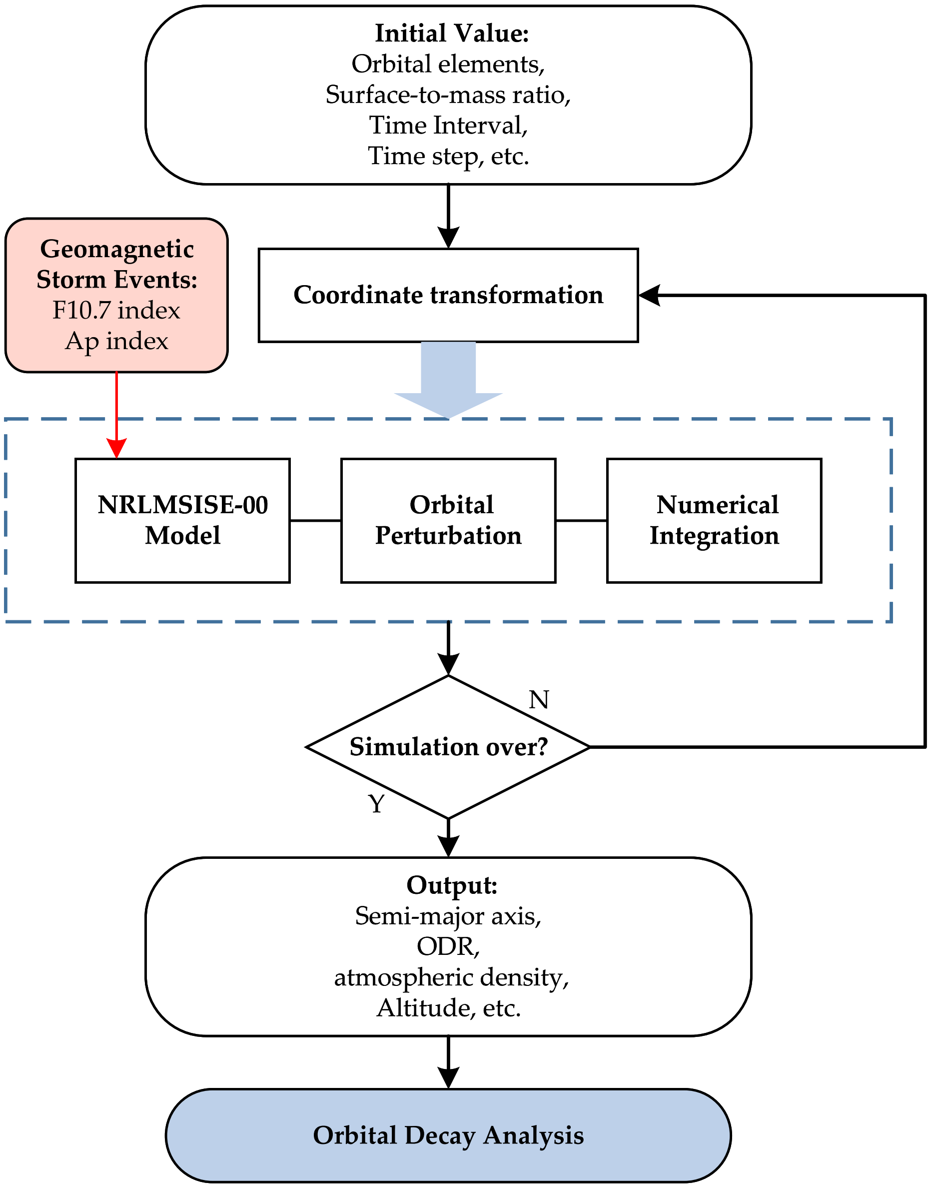


**Figure 2.** Orbital Decay Simulation Procedure.

2.3.1. Satellite Orbital Perturbations

During orbital motion, artificial satellites are subject not only to Earth's gravitational field but also to various perturbing forces. These perturbations can be categorized into two types:

- Conservative perturbations arising from Earth's non-spherical shape and mass inhomogeneity.
- Non-conservative perturbations caused by atmospheric drag, solar radiation pressure, gravitational forces from the Sun and Moon, Earth radiation pressure, and tidal forces.

Under these perturbations, analyzing orbital evolution extends beyond the two-body problem, as orbital elements continuously vary.

The satellite's equation of motion in the equatorial inertial frame is [30]:

$$\ddot{\boldsymbol{r}} = -\frac{\mu}{\boldsymbol{r}^3} + \boldsymbol{a_p} \tag{1}$$

where $\mu$ is Earth's gravitational constant, $\boldsymbol{r}$ is the position vector, and $\boldsymbol{a}_p$ is the resultant acceleration vector from all perturbing forces.

For LEO satellites, dominant perturbations include Earth's non-spherical harmonics and atmospheric drag. Atmospheric drag induces gradual orbital decay. The drag acceleration is given by [31]:

$$\begin{aligned} \boldsymbol{a_F} &= -\frac{1}{2}C_D\frac{A}{m}\rho v_{rel}\boldsymbol{v_{rel}} \\ \boldsymbol{v_{rel}} &= \boldsymbol{v} - \boldsymbol{v_a} \end{aligned} \tag{2}$$

where $C_D$ is the drag coefficient, $A$ is the cross-sectional area projected along the velocity direction, $m$ is the satellite mass, $\rho$ is atmospheric density, $\boldsymbol{v_{rel}}$ is the relative velocity vector between satellite and atmosphere, $v_{rel}$ is its magnitude, $\boldsymbol{v}$ is the satellite's geocentric velocity vector, and $\boldsymbol{v_a}$ is the atmosphere's geocentric velocity vector. The magnitude of drag acceleration is proportional to the satellite's velocity, area-to-mass ratio ($A/m$), and drag coefficient.

#### 2.3.2. NRLMSISE–2.0 Model

The NRLMSISE–2.0 (Naval Research Laboratory Mass Spectrometer and Incoherent Scatter Extended) model is a global empirical reference atmosphere model spanning from Earth's surface to space [32]. It simulates temperature and number density of atmospheric constituents. NRLMSIS–2.0 represents a major upgrade over its predecessor NRLMSISE-00, exhibiting significantly reduced residual bias and standard deviation in predictions.

This study employs NRLMSISE–2.0 to predict atmospheric density along LEO satellite trajectories, enabling computation of drag-induced orbital decay. The model requires the following inputs:

- Day of year;
- Universal Time;
- Altitude;
- Latitude;
- Longitude;
- Local apparent solar time;
- F10.7 index;
- Ap index.

Key outputs include:

- Number densities of: He, O, $N_2$,$O_2$, Ar, H, N and Anomalous oxygen;
- Exospheric temperature;
- Temperature at altitude;
- Total mass density.

Among the inputs, two space weather parameters are critical: the F10.7 index (solar activity proxy) and the Ap index (geomagnetic activity indicator). This work focuses specifically on how drag variations driven by these parameters affect LEO satellite orbits. For orbital perturbation modeling, only the total mass density output is utilized to compute the atmospheric drag perturbation.

#### 2.3.3. Numerical Integration

Two primary methods exist for solving differential equations: analytical methods and numerical integration. For complex orbital dynamics perturbation equations, analytical solutions are often impractical and may lack sufficient accuracy. Therefore, this study employs numerical integration to solve the satellite orbital perturbation equations.

The numerical integration process for orbital perturbations is as follows:

- Initialize: Provide initial satellite position and velocity (typically represented by orbital elements).
- Perturbation Calculation: Compute perturbing accelerations based on the orbital perturbation equations.
- State Propagation: Using a defined step size, numerically propagate the satellite's state (position and velocity) to the next time epoch.
- Iterate: Repeat steps 2–3 to obtain the satellite's trajectory over the desired time period.

In orbital computations, the satellite's position ($\boldsymbol{r}$) and velocity ($\boldsymbol{v}$) are generally expressed in terms of the osculating orbital elements [33]:

$$\begin{aligned} \boldsymbol{r} &= \boldsymbol{r}(a, e, i, \Omega, \omega, M) \\ \boldsymbol{v} = \dot{\boldsymbol{r}} &= \dot{\boldsymbol{r}}(a, e, i, \Omega, \omega, M) \end{aligned} \tag{3}$$

where $a$, $e$, $i$, $\Omega$, $\omega$, and $M$ represent the satellite's semi-major axis, eccentricity, orbital inclination, right ascension of the ascending node (RAAN), argument of perigee, and mean anomaly, respectively.

Within the equatorial inertial frame, perturbing forces acting on the satellite are resolved into three orthogonal, rotating components:

- $\boldsymbol{F_r}$: Radial component (along the geocentric radius vector);
- $\boldsymbol{F_t}$: Transverse component (in the orbital plane, perpendicular to $\boldsymbol{F_r}$);
- $\boldsymbol{F_n}$: Normal component (perpendicular to the orbital plane, completing the right-handed system).

The Gauss planetary equations in terms of these components are [33]:

$$\begin{cases} \dfrac{da}{dt} = \dfrac{2}{n\sqrt{1-e^2}}[F_r e \sin f + F_t(1 + e\cos f)] \\ \dfrac{de}{dt} = \dfrac{\sqrt{1-e^2}}{na}[F_r \sin f + F_t(\cos E + \cos f)] \\ \dfrac{d\Omega}{dt} = \dfrac{r\sin(\omega + f)}{na^2\sqrt{1-e^2}\sin i}F_n \\ \dfrac{di}{dt} = \dfrac{r\cos(\omega + f)}{na^2\sqrt{1-e^2}}F_n \\ \dfrac{d\omega}{dt} = \dfrac{\sqrt{1-e^2}}{nae}\left[-F_r\cos f + F_t\left(\dfrac{2 + e\cos f}{1 + e\cos f}\right)\sin f\right] - \cos i\dfrac{d\Omega}{dt} \\ \dfrac{dM}{dt} = n - \dfrac{1-e^2}{nae}\left[F_r\left(\dfrac{2er}{p} - \cos f\right) + F_t\left(1 + \dfrac{r}{p}\right)\sin f\right] \end{cases} \tag{4}$$

where: $p = a(1-e^2)$ is the semi-latus rectum, $f$ is the true anomaly, $E$ is the eccentric anomaly, and $n = \sqrt{\mu/a^3}$ is the mean motion.

The orbital decay simulations in this study were conducted using a high-precision numerical propagator based on orbital dynamics. The force model accounted for all major perturbations to ensure high fidelity:

- Earth's Gravitational Field: Modeled using the GGM03C geopotential model, complete to degree and order 12.

- Atmospheric Drag: Calculated using the NRLMSISE-00 empirical model, with the satellite's time-varying cross-sectional area and a fixed drag coefficient.
- Solar Radiation Pressure: Considering the satellite's reflectivity coefficient and projected area.
- Third-Body Perturbations: Gravitational effects from the Sun and the Moon.
- Other Perturbations: This includes solid Earth tides and ocean tides, as well as general relativistic effects.

The equations of motion were numerically integrated using a 7/8th-order Runge–Kutta–Fehlberg (RKF78) variable-step algorithm to ensure a balance between computational efficiency and high fidelity. The initial orbital states for the Starlink-like satellite were defined using standard Keplerian elements at the onset of each simulated storm event. By numerically integrating this system of equations, the time evolution of all orbital elements is computed.

## 3. Results and Discussion

Atmospheric drag constitutes the primary factor driving orbital decay in low-Earth-orbit (LEO) satellites. The magnitude of this drag is intrinsically linked to thermospheric density, which exhibits significant variability during geomagnetic storms. Solar radiation serves as the dominant energy source for thermospheric density variations. To investigate the combined effects of geomagnetic storm intensity and solar irradiance on LEO satellite orbital decay during major storm events, we selected representative intense geomagnetic storms occurring since 1965. Simulations based on orbital dynamics models were performed to quantify orbital decay under varying space weather conditions.

### *3.1. Geomagnetic Storm Events Selection*

The United States National Oceanic and Atmospheric Administration (NOAA) categorizes geomagnetic storm intensity into five levels, from G1 to G5 (Table 3). This study focuses on the orbital decay of low-Earth-orbit satellites during intense geomagnetic storms. Consequently, we selected 130 representative historical storm events of G3, G4, and G5 levels occurring between 1965 and 2025, as shown in Tables A1–A3; the distribution across these levels is detailed in Table 3. Figure 3 presents the intensity of these selected storms alongside the solar activity index (monthly average) for the same period. The solar activity index exhibits a clear 11-year periodicity. Notably, a high frequency of intense storms occurred during Solar Cycles 20, 21, and 23 (spanning approximately 1964–2008), primarily during the ascending phase and peak years of solar activity. In contrast, Solar Cycle 24 (2008–2019) was relatively quiescent, with fewer intense storms. Currently, within Solar Cycle 25 (2019–present), the strongest geomagnetic storm in nearly two decades occurred in May 2024, coinciding with the anticipated solar maximum. Figure 3 reveals significant variations in solar irradiance levels during geomagnetic storms of different intensities. Since thermospheric density perturbations exhibit strong dependence on both geomagnetic storm magnitude and solar irradiance, this study specifically investigates the combined effects of these space weather parameters on orbital decay of low-Earth-orbit (LEO) satellites.

**Table 3.** Definition of geomagnetic storm.

| Storm Intensity | Category [a] | Kp Interval [b] | Dst Interval [c] | Number of Events |
|---|---|---|---|---|
| Minor | G1 | Kp = 5 | Dst $\geq -50$ nT | / |
| Moderate | G2 | Kp = 6 | $-100 \leq$ Dst $< -50$ nT | / |
| Strong | G3 | Kp = 7 | $-150 \leq$ Dst $< -100$ nT | 50 |
| Severe | G4 | Kp = 8 | $-250 \leq$ Dst $< -150$ nT | 59 |
| Extreme | G5 | Kp = 9 | Dst $\leq -250$ nT | 21 |
| – | – | – | – | Total: 130 events |

[a] Following the NOAA's nomenclature. [b] The definition of storm intensity by Kp index following NOAA. [c] This definition of storm intensity intervals is arbitrary.

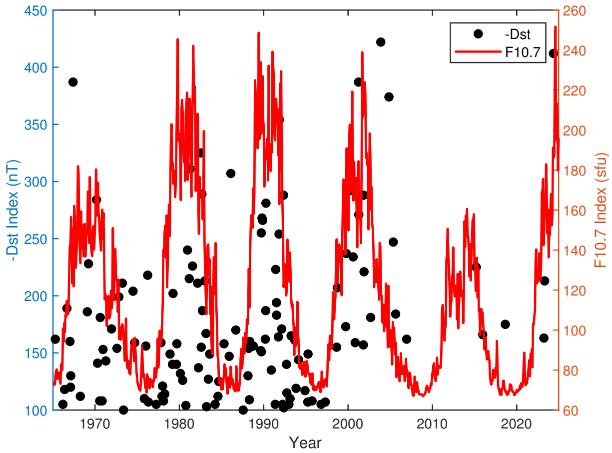


**Figure 3.** Minimum Dst index of selected storms and F10.7 index (monthly average) for the same period.

### *3.2. Configuration of Satellite Orbital Parameters*

To investigate the coupled effects of geomagnetic storm intensity and solar irradiance on LEO satellite orbital decay, we conducted numerical simulations using a representative satellite model. The orbital parameters were configured with reference to Starlink satellite characteristics (mean altitude: 350 km, inclination: 53°, complete parameters in Table 4). This choice is justified for several reasons. First, with thousands of satellites deployed, Starlink constitutes the largest and most prominent LEO constellation to date, making it a highly relevant and representative case study for investigating orbit decay challenges. Second, its operational altitude (around 550 km) and inclination (approximately 53°) are typical for many proposed and existing constellations, placing the findings of this study in a context of immediate operational interest. Finally, while the absolute decay rates are satellite-specific (depending on mass-to-area ratio), the fundamental physical responses to solar irradiance and geomagnetic activity investigated here are governed by atmospheric density changes and are thus broadly applicable to all satellites in similar orbital regimes. Focusing on a Starlink-like satellite therefore enhances the practical relevance of our results without loss of generality regarding the underlying physical mechanisms. To ensure controlled comparisons, all simulations maintained identical temporal windows spanning 3 days centered on storm events, comprising:

- Pre-storm phase: 24 h preceding storm onset;
- Main phase: 24 h during peak geomagnetic activity;
- Recovery phase: 24 h post-peak.

Using the March 1966 geomagnetic storm event as a representative case (Figure 4), the temporal evolution exhibited: Storm commencement (13 March: initial phase), Peak intensity (14 March: Dst = $-105$ nT at 6:00 UT), Gradual recovery(15 March). The simulation window was precisely defined from 13 March 00:00:00 UT to 16 March 00:00:00 UT, encompassing all critical storm phases.

**Table 4.** Definition of geomagnetic storm.

| Parameter Name | Value |
|---|---|
| Time interval | 72 h (seen in Figure 4) |
| Time step | 30 s |
| Area-to-Mass ratio | $0.0165\,m^2/kg$ |
| Inclination | 53.1596° |
| Position in ECI [a] | $(-640.4135501, -4065.221042, 5330.232267)$ km |
| Velocity in ECI | $(7.273360727, -2.338354621, -0.909030324)$ km/s |

[a] ECI: Earth Centered Inertial Coordinates.

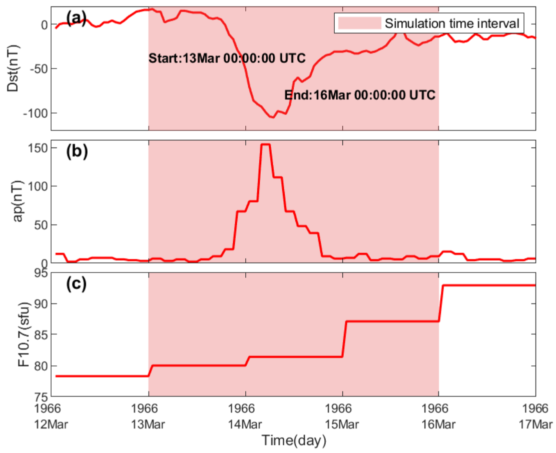


**Figure 4.** Multivariate space weather parameters evolution during 12–18 March 1966: (**a**) Dst index, (**b**) ap index, (**c**) F10.7 solar flux. The pink-shaded temporal window indicates the simulation period.

### *3.3. Experiments and Analysis*

#### 3.3.1. Effects of Magnetic Storms on LEO Satellite

Analysis of the 15 May 2005 geomagnetic storm event ($Dst_{min}$ = −223 nT, classified as severe) reveals significant orbital decay effects on low-Earth-orbit satellites through numerical simulations (Figure 5). Key parameters tracked during the storm include: geomagnetic indices (Dst, Ap), solar flux (F10.7), local thermospheric density, orbital altitude variation (quantified by semi-major axis), and Orbital decay rate ($da/dt$). Critically, solar irradiance remained stable throughout the event, effectively isolating geomagnetically-driven thermospheric density perturbations as the dominant decay mechanism. The observed strong Ap-density correlation aligns with the ap-index parameterization in the NRLMSISE-2.0 atmospheric model. Pre-storm thermospheric density stabilized at $10^{-11}$ kg/m$^3$, surged by 340% during peak storm conditions, and settled at an elevated baseline post-recovery. Concomitantly, semi-major axis reduction accelerated substantially, with maximum decay (695.09 m) occurring during peak storm intensity, exceeding pre-storm (515.16 m) and recovery-phase (554.77 m) losses. The orbital decay rate (ODR) similarly peaked during maximum geomagnetic disturbance. This demonstrates that for high area-to-mass ratio LEO satellites (e.g., Starlink with large solar arrays) at 300–400 km altitudes, unmitigated storm exposure causes rapid orbital decay through atmospheric drag acceleration, potentially reducing operational lifetime in severe storm event without autonomous station-keeping maneuvers.

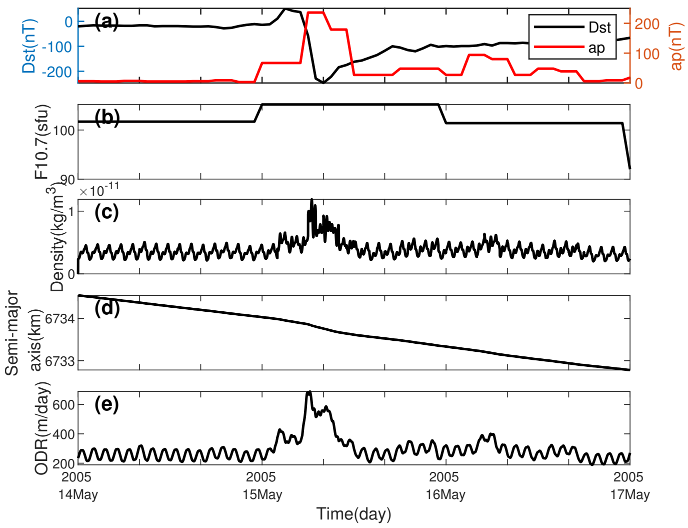


**Figure 5.** Multivariate space weather and Orbital parameters evolution during 14–17 May 2005: (**a**) Dst index and ap index, (**b**) F10.7 solar flux, (**c**) Local thermospheric density, (**d**) Semi-major axis, (**e**) The orbital decay rate (ODR).

### 3.3.2. Analysis of Combined Effects of Geomagnetic Storm Intensity and Solar Irradiance on LEO Satellite Orbital Decay

We conducted numerical simulations of orbital decay for 130 representative geomagnetic storm events. Through systematic modeling, we quantified the orbital decay magnitude during each storm and performed statistical analysis. As shown in Figure 6, the relationship between the minimum Dst index ($Dst_{min}$) and orbital decay reveals an overall tendency where stronger storms generally correspond to greater decay magnitudes. However, the correlation remains moderate, primarily due to significant variations in solar irradiance levels across different storm events—a critical secondary factor influencing thermospheric density. Detailed examination of storms with $Dst_{min} > -200$ nT (Figure 6) shows: (1) wide dispersion of solar flux values (F10.7 range: 65–210 sfu); (2) comprehensive coverage of solar activity levels (G1–G5); and (3) clear positive correlation between solar activity class and decay magnitude. This solar influence explains the weakened storm intensity–decay relationship, demonstrating that orbital decay is jointly governed by geomagnetic storm intensity (primary short-term driver) and solar irradiance level (dominant background modulator).

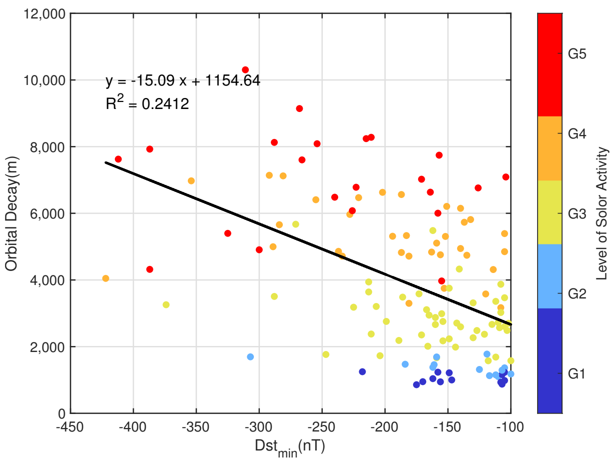


**Figure 6.** Scatter plots of geomagnetic storm intensity ($Dst_{min}$) versus satellite orbital decay magnitude. Color gradient indicates solar activity levels: dark blue (G1), light blue (G2), yellow (G3), orange (G4), red (G5). Black curve denotes regression fit.

Figure 7 presents the semi-major axis decay of satellites during 72-h periods across different classes of geomagnetic storms. Panel (a) displays the orbital decay trajectories for all storm events, revealing progressively diverging decay patterns over time. This divergence stems from two primary factors:

- Orbital Altitude Effects. Lower orbits experience exponentially higher local thermospheric density, and atmospheric drag forces increase substantially, which accelerates decay rates, leading to greater cumulative decay.
- Solar Irradiance Influence. Variable F10.7 flux across storms modifies background thermospheric density, and higher solar activity elevates baseline density, enhancing decay rates.

As evidenced in Figure 6, strong (G3) and severe (G4) storms exhibit significant solar flux variability, while extreme (G5) events show more consistent irradiance levels. This explains why panels (b)–(d) in Figure 7 demonstrate larger decay dispersion in strong/severe storms and tighter clustering in extreme events.

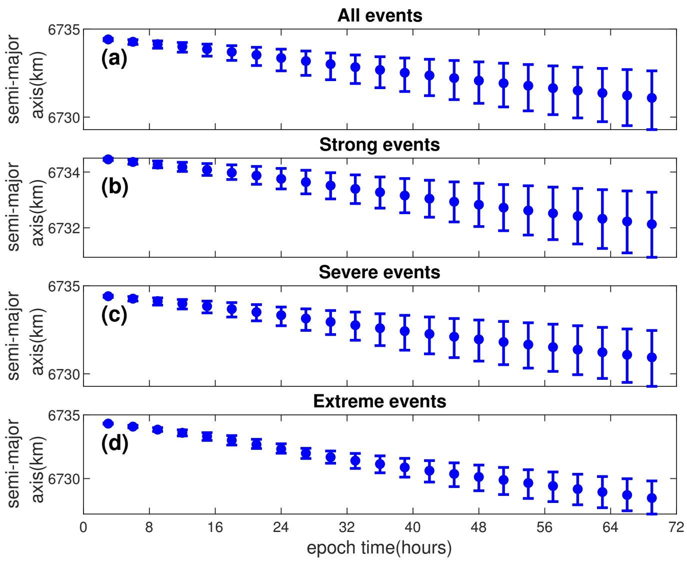


**Figure 7.** Temporal evolution of satellite semi-major axis decay under different levels of geomagnetic storm (130 Case Studies): (**a**) All events, (**b**) Strong events, (**c**) Severe events, (**d**) Extreme events. The error bars indicate 25th percentiles (lower edge) and 75th percentiles (upper edge).

To investigate the influence of solar irradiance on low-Earth-orbit (LEO) satellite orbital decay, with a specific focus on its dominant influence during geomagnetic storms, we analyzed the relationship between the average solar radio flux ($F10.7_{mean}$) and decay magnitude, as shown in Figure 8. The results reveal a strong positive correlation ($R^2 = 0.8388$), particularly evident across G1–G4 solar activity levels. Specifically: storms with G1–G2 level irradiance ($F10.7 < 100$ sfu) typically induced orbital decay below 2 km; G3–level events (100–150 sfu) caused 2-4 km decay; G4-level activity (150–200 sfu) led to 4–8 km decay; while G5-level storms ($F10.7 > 200$ sfu) consistently produced over 6 km decay. This demonstrates that solar irradiance—by modulating background thermospheric density—serves as the dominant factor governing orbital decay during geomagnetic storms, with higher flux levels systematically exacerbating atmospheric drag effects. We further compared the average solar irradiance ($F10.7_{mean}$) with satellite orbital decay magnitude across different geomagnetic storm phases (initial, main, and recovery), as shown in Figure 9. The results demonstrate a statistically significant positive correlation between orbital decay and solar irradiance during all three phases. This confirms the stable, governing role of solar radiation as the background energy source—it not only establishes the decay baseline during quiet periods but also continuously determines the thermospheric density magnitude throughout the entire storm process, thereby controlling the total decay amount.

To visually illustrate the relative importance of solar radiation and geomagnetic activity in orbital decay, we selected several representative cases for comparative analysis, as shown in Table 5. A notable observation is that a moderate-intensity magnetic storm during high solar activity (e.g., the October 2001 event, $Dst_{\mathrm{min}} = -157$ nT) resulted in an orbital decay of up to 7744 m, whereas an exceptionally intense magnetic storm during low solar activity (e.g., the February 1986 event, $Dst_{\mathrm{min}} = -307$ nT) caused only 1694 m of decay. The decay in the former case is approximately 4.5 times greater than that in the latter. This striking contrast conclusively demonstrates that the background solar radiation level ($F_{10.7}$) is the dominant factor determining the total orbital decay, exerting a far greater influence than the peak intensity of an individual magnetic storm ($Dst_{\mathrm{min}}$). Physically, this is because solar extreme ultraviolet radiation sets the baseline level of thermospheric atmospheric density, while geomagnetic disturbances act as transient modulations superimposed on this baseline. Therefore, even an extremely intense geomagnetic storm occurring during a period of low solar activity can only inject energy into an already tenuous atmospheric environment, ultimately resulting in limited total orbital decay.

**Table 5.** Comparative Cases Demonstrating Solar Irradiance Dominance over Storm Intensity in Orbital Decay.

| Date Range | $Dst_{min}$ (nT) | F10.7$_{mean}$ (sfu) | Solar Activity | Orbital Decay (m) |
|---|---|---|---|---|
| 10–13 October 1980 | −104.0 | 241.3 | High | 7089 |
| 15–18 February 1980 | −132.0 | 199.6 | High | 5813 |
| 24–27 May 1980 | −126.0 | 281.6 | High | 6762 |
| 16–19 May 1991 | −105.0 | 177.2 | High | 5391 |
| 27–30 October 2001 | −157.0 | 229.8 | High | 7744 |
| 8–11 February 1986 | −307.0 | 96.0 | **Low** | **1694** |
| 31 March–3 April 1976 | −218.0 | 79.8 | **Low** | **1247** |

Note: Bold rows highlight intense storms during solar minimum that produced significantly less decay than weaker storms during solar maximum.

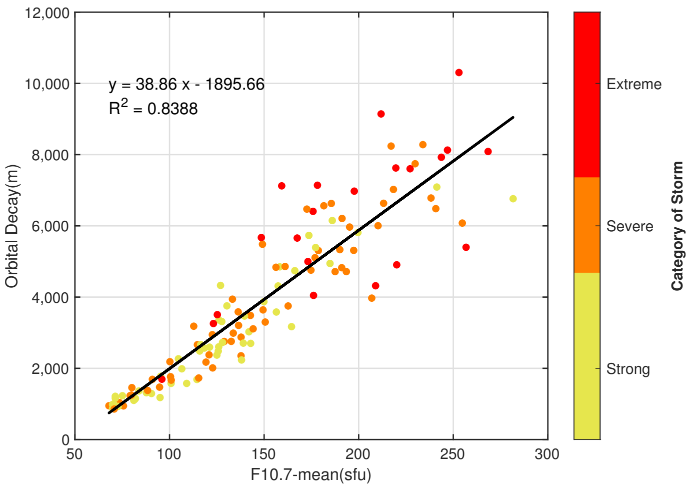


**Figure 8.** Scatter plots of solar activity (F10.7$_{mean}$) versus satellite orbital decay magnitude. Color gradient indicates geomagnetic storm levels: yellow (Strong), orange (Severe), red (Extreme). Black curve denotes regression fit.

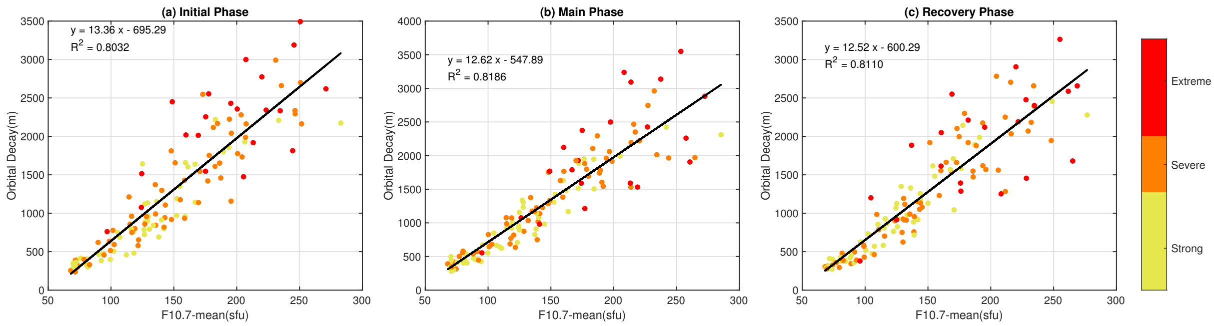


**Figure 9.** Scatter plots of solar activity ($F10.7_{mean}$) versus satellite orbital decay during different geomagnetic storm phases. (**a**) Initial, (**b**) Main, (**c**) Recovery.

To investigate the coupled effects of geomagnetic storm intensity and solar irradiance on LEO satellite orbital decay, we performed multivariate linear regression analysis of 130 storm events, incorporating both solar flux (F10.7) and geomagnetic index (Dst) as predictors (Figures 10 and 11). The fitted model achieved a correlation coefficient of 0.8641, revealing solar activity as the dominant driver compared to geomagnetic effects. This predominance stems from two physical mechanisms: (1) orbital decay being a cumulative process primarily dependent on background thermospheric density, which is predominantly modulated by solar extreme ultraviolet radiation, and (2) geomagnetic disturbances causing transient density enhancements that temporarily accelerate decay rates. Consequently, effective orbit maintenance strategies during storms require simultaneous monitoring of both F10.7 trends (for long-term density variations) and Dst/Ap indices (for short-term drag spikes), with autonomous propulsion systems recommended to compensate for the compound effects, particularly for high area-to-mass ratio satellites below 400 km altitude. Our findings are well-grounded in prior empirical research. They are consistent with the long-term density trends derived from orbital data by Doornbos et al. [34] and are complemented by the work of Khodairy et al. [30], which physically explains how solar EUV and X-ray radiation profoundly impact the thermosphere. This consistency between our large-scale statistical model and established observational studies strengthens the credibility of our key conclusion that operational strategies must account for both solar irradiance and geomagnetic activity.

While this study has focused on the roles of solar irradiance and geomagnetic activity, it is important to acknowledge that other factors also influence LEO satellite orbital decay. The ballistic coefficient (often represented as mass-to-cross-sectional area ratio, $m/C_D A$) is a primary satellite-specific parameter. A satellite with a lower ballistic coefficient (e.g., larger cross-sectional area or lower mass) will experience greater atmospheric drag and faster decay for the same atmospheric density conditions. Furthermore, orbital parameters such as eccentricity and argument of perigee play a significant role. The core findings of this study—that solar irradiance dominates the long-term decay magnitude and geomagnetic activity controls short-term rates—are based on the fundamental driver of these processes: thermospheric density. The factors mentioned above modulate the satellite's response to a given density environment, but solar and geomagnetic activity are the dominant forcings that alter the environment itself. Therefore, the relative importance of solar versus geomagnetic drivers identified here provides a crucial foundational layer. Future work could integrate these satellite-specific and orbital parameters to develop even more precise, targeted decay models for individual satellite missions.

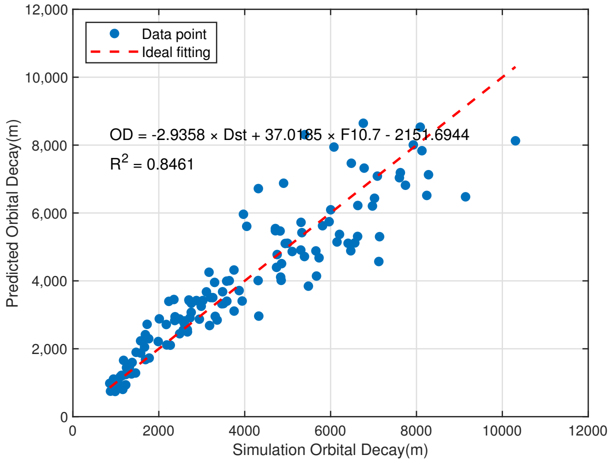


**Figure 10.** The fitting effect diagram of the orbital decay values of 130 satellites during magnetic storm events and the solar activity index F10.7 and geomagnetic index Dst during the magnetic storm period.

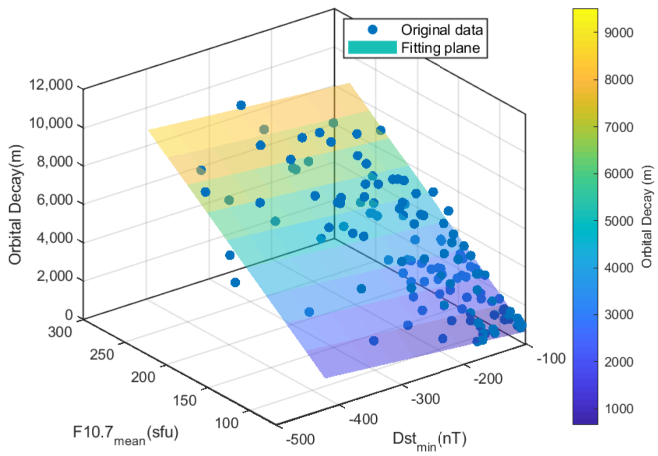


**Figure 11.** 3D fitting effect diagram of 130 satellite orbital decay values for magnetic storm events and the solar activity index F10.7 and geomagnetic index Dst during the magnetic storm.The fitting plane is colored according to the predicted orbital decay value (see color bar).

## 4. Conclusions

In this study, we selected 130 representative intense geomagnetic storm events from 1965 to 2025 and conducted 72-h orbital simulations for low-Earth-orbit (LEO) satellites using orbital dynamics models. Our analysis focused on the combined effects of solar irradiance and geomagnetic storm intensity on LEO satellite orbital decay. The main findings are as follows.

During geomagnetic storms, solar irradiance serves as the primary energy source for changes in background thermospheric density, influencing its magnitude and thereby determining the extent of orbital decay of LEO satellites. In contrast, geomagnetic activity primarily affects the short-term orbital decay rate of LEO satellites by heating the upper atmosphere through transient disturbances, leading to abrupt changes in thermospheric density. Compared to storm intensity, solar radiation intensity shows a stronger correlation with satellite orbital decay. The underlying mechanism is that orbital decay depends on the long-term accumulation of the average magnitude of thermospheric density. As solar irradiance is the main regulator of background thermospheric density, it constitutes the dominant factor influencing orbital decay of LEO satellites, which is consistent with our experimental findings.

For LEO satellites operating during geomagnetic storms, comprehensive consideration of both solar irradiance and geomagnetic activity is essential for accurate orbital decay prediction, which is crucial for orbit maintenance strategies. Our results provide a basis for re-evaluating operational priorities. Since solar irradiance is shown to dominate the total decay amount during geomagnetic storms, our findings lend support to strategies that consider the persistent background level of solar activity as a primary factor, with transient storm intensity serving as a secondary but important input. This perspective highlights that cumulative decay from recurrent storms could be substantially greater during solar maximum than during solar minimum. Accordingly, we propose that long-term fuel budgeting guided by solar cycle forecasts forms a robust foundational strategy, supplemented by short-term alerts based on real-time geomagnetic activity.

**Author Contributions:** Conceptualization, H.Y., L.C. and B.C.; methodology, H.Y., L.C. and B.C.; formal analysis, H.Y., L.C. and B.C.; software, H.Y. and L.C.; validation, H.Y., L.C. and B.C.; investigation, L.C.; resources, L.C. and B.C.; data curation, H.Y.; writing—original draft preparation, H.Y.; writing—review and editing, H.Y., L.C. and B.C.; visualization, H.Y.; supervision, L.C. and B.C.; project administration, B.C.; funding acquisition, B.C. All authors have read and agreed to the published version of the manuscript.

**Funding:** This research was funded by the National Key Research and Development Program of China, grant number 2022YFF0503900; the National Key Research and Development Program of China, grant number 2022YFD2401200; the Shenzhen Higher Education Institutions Stabilization Support Program Project, grant number GXWD20220811163556003; the National Natural Science Foundation of China, grant number NSFC62202127; the National Natural Science Foundation of Shenzhen, grant number JCYJ20241202123731040.

**Data Availability Statement:** Data are contained within the article.

**Acknowledgments:** We gratefully acknowledge the use of space weather data from the NASA's Goddard Space Flight Center (https://spdf.gsfc.nasa.gov/), accessed on 20 October 2025.

**Conflicts of Interest:** The authors declare no conflicts of interest.

## Appendix A

The complete list of 130 geomagnetic storm events used in our statistical analysis is provided in Tables A1–A3. The simulation period for each event spanned three days centered on the storm onset.

**Table A1.** List of geomagnetic storm events analyzed in this study (Part 1 of 3).

| Date Range | $Dst_{min}$ (nT) | $F10.7_{mean}$ (sfu) |
|---|---|---|
| 17–20 April 1965 | −162.0 | 73.4 |
| 13–16 March 1966 | −105.0 | 83.8 |
| 25–28 May 1966 | −118.0 | 109.1 |
| 3–6 September 1966 | −189.0 | 100.2 |
| 13–16 January 1967 | −160.0 | 137.8 |
| 15–18 February 1967 | −130.0 | 127.6 |
| 7–10 February 1967 | −120.0 | 156.5 |
| 5–8 April 1968 | −112.0 | 126.1 |
| 2–5 February 1969 | −186.0 | 142.8 |
| 6–9 November 1970 | −108.0 | 149.9 |
| 13–16 December 1970 | −153.0 | 162.7 |
| 21–24 April 1970 | −141.0 | 127.0 |
| 24–27 July 1970 | −108.0 | 164.5 |

**Table A1.** *Cont.*

| Date Range | $Dst_{min}$ (nT) | $F10.7_{mean}$ (sfu) |
|---|---|---|
| 16–19 August 1970 | −181.0 | 150.6 |
| 17–20 December 1971 | −171.0 | 137.8 |
| 14–17 April 1971 | −143.0 | 139.0 |
| 8–11 August 1972 | −154.0 | 119.3 |
| 20–23 May 1973 | −100.0 | 100.8 |
| 15–18 September 1974 | −159.0 | 100.9 |
| 8–11 November 1975 | −110.0 | 81.1 |
| 10–13 January 1976 | −156.0 | 75.7 |
| 2–5 May 1976 | −107.0 | 71.3 |
| 27–30 October 1977 | −159.0 | 90.9 |
| 10–13 December 1977 | −112.0 | 114.5 |
| 6–9 April 1977 | −105.0 | 75.1 |
| 4–7 January 1978 | −121.0 | 125.0 |
| 24–27 November 1978 | −149.0 | 130.3 |
| 14–17 February 1978 | −108.0 | 142.0 |
| 10–13 April 1978 | −114.0 | 157.4 |
| 10–13 March 1979 | −140.0 | 186.0 |
| 29 August–1 September 1979 | −140.0 | 184.8 |
| 17–20 September 1979 | −158.0 | 210.2 |
| 10–13 October 1980 | −104.0 | 241.3 |
| 15–18 February 1980 | −132.0 | 199.6 |
| 24–27 May 1980 | −126.0 | 281.6 |
| 9–12 April 1982 | −137.0 | 173.7 |
| 06–09 August 1982 | −155.0 | 206.9 |
| 26–29 September 1982 | −187.0 | 191.0 |
| 1–4 March 1983 | −167.0 | 144.2 |
| 24–27 March 1983 | −103.0 | 115.9 |
| 12–15 June 1983 | −127.0 | 125.8 |
| 7–10 August 1983 | −149.0 | 138.1 |
| 28–31 March 1984 | −105.0 | 139.6 |
| 31 July–3 August 1984 | −112.0 | 82.0 |

**Table A2.** List of geomagnetic storm events analyzed in this study (Part 2 of 3).

| Date Range | $Dst_{min}$ (nT) | $F10.7_{mean}$ (sfu) |
|---|---|---|
| 4–7 September 1984 | −125.0 | 87.8 |
| 29 November–2 December 1985 | −147.0 | 70.5 |
| 20–23 April 1985 | −158.0 | 79.2 |
| 11–14 September 1986 | −170.0 | 68.0 |
| 28–31 July 1987 | −100.0 | 95.0 |
| 9–12 October 1988 | −156.0 | 174.8 |
| 21–24 February 1988 | −130.0 | 104.7 |
| 26–29 March 1988 | −154.0 | 128.9 |
| 21–24 April 1988 | −109.0 | 118.4 |
| 5–8 May 1988 | −160.0 | 114.7 |
| 28–31 August 1989 | −152.0 | 178.7 |
| 26–29 September 1989 | −151.0 | 191.2 |
| 27–30 November 1990 | −135.0 | 166.2 |
| 12–15 March 1990 | −162.0 | 149.1 |
| 29 March–1 April 1990 | −187.0 | 181.6 |
| 16–19 May 1991 | −105.0 | 177.2 |
| 13–16 July 1991 | −183.0 | 190.0 |
| 8–11 July 1991 | −194.0 | 197.4 |

**Table A2.** *Cont.*

| Date Range | $Dst_{min}$ (nT) | F10.7$_{mean}$ (sfu) |
|---|---|---|
| 1–4 October 1991 | −164.0 | 213.2 |
| 28–31 December 1992 | −105.0 | 126.0 |
| 20–23 February 1992 | −171.0 | 218.4 |
| 2–5 April 1992 | −105.0 | 158.3 |
| 21–24 May 1992 | −102.0 | 142.9 |
| 16–19 September 1992 | −140.0 | 121.2 |
| 28 September–1 October 1992 | −115.0 | 116.5 |
| 3–6 November 1993 | −119.0 | 95.3 |
| 16–19 February 1993 | −110.0 | 128.0 |
| 4–7 April 1993 | −165.0 | 122.6 |
| 12–15 September 1993 | −161.0 | 80.1 |
| 25–28 November 1994 | −117.0 | 81.7 |
| 21–24 February 1994 | −144.0 | 106.5 |
| 25–28 March 1995 | −107.0 | 90.5 |
| 6–9 April 1995 | −149.0 | 71.3 |
| 27–30 September 1995 | −108.0 | 72.9 |
| 22–25 October 1996 | −105.0 | 69.9 |
| 21–24 April 1997 | −107.0 | 69.9 |
| 26–29 August 1998 | −155.0 | 133.7 |
| 22–25 September 1999 | −173.0 | 136.3 |
| 6–9 November 2000 | −159.0 | 176.9 |
| 27–30 October 2001 | −157.0 | 229.8 |
| 7–10 September 2002 | −181.0 | 193.5 |
| 24–27 August 2005 | −184.0 | 94.7 |
| 14–17 December 2006 | −162.0 | 88.4 |
| 20–23 December 2015 | −166.0 | 122.8 |

**Table A3.** List of geomagnetic storm events analyzed in this study (Part 3 of 3).

| Date Range | $Dst_{min}$ (nT) | F10.7$_{mean}$ (sfu) |
|---|---|---|
| 25–28 August 2018 | −175.0 | 70.8 |
| 23–26 March 2023 | −163.0 | 156.3 |
| 25–28 May 1967 | −387.0 | 208.9 |
| 23–26 March 1969 | −228.0 | 195.2 |
| 8–11 March 1970 | −284.0 | 167.5 |
| 31 October–3 November 1972 | −199.0 | 132.6 |
| 1–4 April 1973 | −211.0 | 120.9 |
| 5–8 July 1974 | −204.0 | 115.4 |
| 31 March–3 April 1976 | −218.0 | 79.8 |
| 3–6 April 1979 | −202.0 | 185.5 |
| 19–22 December 1980 | −240.0 | 240.8 |
| 5–8 March 1981 | −215.0 | 217.1 |
| 12–15 April 1981 | −311.0 | 253.0 |
| 25–28 July 1981 | −226.0 | 254.8 |
| 1–4 March 1982 | −211.0 | 233.9 |
| 13–16 July 1982 | −325.0 | 256.8 |
| 6–9 September 1982 | −289.0 | 173.2 |
| 9–12 January 1983 | −213.0 | 149.4 |
| 8–11 February 1986 | −307.0 | 96.0 |
| 20–23 October 1989 | −268.0 | 211.8 |
| 17–20 November 1989 | −266.0 | 227.2 |
| 19–22 September 1989 | −255.0 | 175.9 |
| 10–13 April 1990 | −281.0 | 159.3 |

**Table A3.** *Cont.*

| Date Range | $Dst_{min}$ (nT) | $F10.7_{mean}$ (sfu) |
|---|---|---|
| 28–31 October 1991 | −254.0 | 268.4 |
| 8–11 November 1991 | −354.0 | 197.7 |
| 5–8 June 1991 | −223.0 | 238.2 |
| 10–13 May 1992 | −288.0 | 125.3 |
| 24–27 September 1998 | −207.0 | 136.5 |
| 21–24 October 1999 | −237.0 | 161.1 |
| 6–9 April 2000 | −292.0 | 178.2 |
| 15–18 July 2000 | −300.0 | 220.1 |
| 11–14 August 2000 | −234.0 | 187.5 |
| 24–27 November 2001 | −221.0 | 172.6 |
| 5–8 November 2001 | −288.0 | 246.9 |
| 31 March–3 April 2001 | −387.0 | 243.7 |
| 11–14 April 2001 | −271.0 | 148.5 |
| 20–23 November 2003 | −422.0 | 176.1 |
| 8–11 November 2004 | −374.0 | 123.2 |
| 14–17 May 2005 | −247.0 | 100.5 |
| 17–20 March 2015 | −225.0 | 112.8 |
| 23–26 April 2023 | −213.0 | 133.3 |
| 10–13 May 2024 | −412.0 | 219.6 |

## References

1. Dreher, P.; Little, R.; Wittenstein, G. Skylab Orbital Lifetime Prediction and Decay Analysis; NASA Technical Memorandum 78308. 1980. Available online: https://ntrs.nasa.gov/api/citations/19810005468/downloads/19810005468.pdf (accessed on 20 October 2025)
2. Nwankwo, V.U.; Chakrabarti, S.K. Theoretical model of drag force impact on a model international space station satellite due to solar activity. *Trans. Jpn. Soc. Aeronaut. Space Sci. Aerosp. Technol. Jpn.* **2014**, *12*, 47–53. [CrossRef]
3. Baruah, Y.; Roy, S.; Sinha, S.; Palmerio, E.; Pal, S.; Oliveira, D.M.; Nandy, D. The loss of Starlink satellites in February 2022: How moderate geomagnetic storms can adversely affect assets in low-Earth orbit. *Space Weather* **2024**, *22*, e2023SW003716. [CrossRef]
4. Hedin, A.; Mayr, H. Solar EUV induced variations in the thermosphere. *J. Geophys. Res. Atmos.* **1987**, *92*, 869–875. [CrossRef]
5. Nwankwo, V.U. Space weather: Response of the atmosphere to solar activity and its implications for LEO satellites aerodynamic drag. In *Exploring the Universe: From Near Space to Extra-Galactic: A Collection of Research Reviews on Contemporary Astrophysics and Space Science*; Springer: Berlin/Heidelberg, Germany, 2018; pp. 637–644.
6. Qian, L.; Solomon, S.C. Thermospheric density: An overview of temporal and spatial variations. *Space Sci. Rev.* **2012**, *168*, 147–173. [CrossRef]
7. Emmert, J.T. Thermospheric mass density: A review. *Adv. Space Res.* **2015**, *56*, 773–824. [CrossRef]
8. Emmert, J. Altitude and solar activity dependence of 1967–2005 thermospheric density trends derived from orbital drag. *J. Geophys. Res. Space Phys.* **2015**, *120*, 2940–2950. [CrossRef]
9. Jun, N.; Hanxian, F.; Libin, W. Correlations between solar activity and thermospheric density. *Chin. J. Space Sci.* **2014**, *34*, 73–80. [CrossRef]
10. Eastes, R.; Bailey, S.; Bowman, B.; Marcos, F.; Wise, J.; Woods, T. The correspondence between thermospheric neutral densities and broadband measurements of the total solar soft X-ray flux. *Geophys. Res. Lett.* **2004**, *31*, L19804. [CrossRef]
11. Rhoden, E.; Forbes, J.; Marcos, F. The influence of geomagnetic and solar variabilities on lower thermosphere density. *J. Atmos. Sol.-Terr. Phys.* **2000**, *62*, 999–1013. [CrossRef]
12. Le, H.; Liu, L.; Wan, W. An analysis of thermospheric density response to solar flares during 2001–2006. *J. Geophys. Res. Space Phys.* **2012**, *117*, A03307. [CrossRef]
13. Huang, Y.; Richmond, A.D.; Deng, Y.; Chamberlin, P.C.; Qian, L.; Solomon, S.C.; Roble, R.G.; Xiao, Z. Wavelength dependence of solar irradiance enhancement during X-class flares and its influence on the upper atmosphere. *J. Atmos. Sol.-Terr. Phys.* **2014**, *115*, 87–94. [CrossRef]
14. Kalafatoglu Eyiguler, E.; Kaymaz, Z.; Frissell, N.A.; Ruohoniemi, J.; Rastätter, L. Investigating upper atmospheric Joule heating using cross-combination of data for two moderate substorm cases. *Space Weather* **2018**, *16*, 987–1012. [CrossRef]
15. Richmond, A.; Matsushita, S. Thermospheric response to a magnetic substorm. *J. Geophys. Res.* **1975**, *80*, 2839–2850. [CrossRef]

16. Oliveira, D.; Zesta, E.; Schuck, P.; Sutton, E. Thermosphere global time response to geomagnetic storms caused by coronal mass ejections. *J. Geophys. Res. Space Phys.* **2017**, *122*, 10762–10782. [CrossRef]
17. Kim, K.H.; Moon, Y.J.; Cho, K.S.; Kim, H.D.; Park, J.Y. Atmospheric drag effects on the KOMPSAT-1 satellite during geomagnetic superstorms. *Earth Planets Space* **2006**, *58*, e25–e28. [CrossRef]
18. Oliveira, D.M.; Zesta, E. Satellite orbital drag during magnetic storms. *Space Weather* **2019**, *17*, 1510–1533. [CrossRef]
19. Chen, G.m.; Xu, J.; Wang, W.; Lei, J.; Burns, A.G. A comparison of the effects of CIR-and CME-induced geomagnetic activity on thermospheric densities and spacecraft orbits: Case studies. *J. Geophys. Res. Space Phys.* **2012**, *117*, 8315.
20. Oliveira, D.M.; Zesta, E.; Hayakawa, H.; Bhaskar, A. Estimating satellite orbital drag during historical magnetic superstorms. *Space Weather* **2020**, *18*, e2020SW002472. [CrossRef]
21. Li, R.; Lei, J. The determination of satellite orbital decay from POD data during geomagnetic storms. *Space Weather* **2021**, *19*, e2020SW002664. [CrossRef]
22. Zhang, K.; Li, X.; Xiong, C.; Meng, X.; Li, X.; Yuan, Y.; Zhang, X. The influence of geomagnetic storm of 7-8 September 2017 on the Swarm precise orbit determination. *J. Geophys. Res. Space Phys.* **2019**, *124*, 6971–6984. [CrossRef]
23. Oliveira, D.M.; Zesta, E.; Nandy, D. The 10 October 2024 geomagnetic storm may have caused the premature reentry of a Starlink satellite. *Front. Astron. Space Sci.* **2025**, *11*, 1522139. [CrossRef]
24. Oliveira, D.M.; Zesta, E.; Garcia-Sage, K. Tracking reentries of Starlink satellites during the rising phase of solar cycle 25. *Front. Astron. Space Sci.* **2025**, *12*, 1572313. [CrossRef]
25. Fang, T.W.; Kubaryk, A.; Goldstein, D.; Li, Z.; Fuller-Rowell, T.; Millward, G.; Singer, H.J.; Steenburgh, R.; Westerman, S.; Babcock, E. Space weather environment during the SpaceX Starlink satellite loss in February 2022. *Space Weather* **2022**, *20*, e2022SW003193. [CrossRef]
26. Dang, T.; Li, X.; Luo, B.; Li, R.; Zhang, B.; Pham, K.; Ren, D.; Chen, X.; Lei, J.; Wang, Y. Unveiling the space weather during the Starlink satellites destruction event on 4 February 2022. *Space Weather* **2022**, *20*, e2022SW003152. [CrossRef]
27. Tapping, K. The 10.7 cm solar radio flux (F10. 7). *Space Weather* **2013**, *11*, 394–406. [CrossRef]
28. Hathaway, D.H. The solar cycle. *Living Rev. Sol. Phys.* **2015**, *12*, 4. [CrossRef] [PubMed]
29. Rostoker, G. Geomagnetic indices. *Rev. Geophys.* **1972**, *10*, 935–950. [CrossRef]
30. Khodairy, S.; Sharaf, M.; Awad, M.; Hamed, R.A.; Hussein, M. Impact of solar activity on low earth orbiting satellites. *J. Phys. Conf. Ser.* **2020**, *1523*, 012010. [CrossRef]
31. Doornbos, E.; Förster, M.; Fritsche, B.; van Helleputte, T.; van den IJssel, J.; Koppenwallner, G.; Lühr, H.; Rees, D.; Visser, P.; Kern, M. Air density models derived from multi-satellite drag observations. In Proceedings of the ESAS Second Swarm International Science Meeting, Potsdam, Germany, 24–26 June 2009; Volume 24.
32. Picone, J.M.; Hedin, A.E.; Drob, D.P.; Aikin, A.C. NRLMSISE-00 empirical model of the atmosphere: Statistical comparisons and scientific issues. *J. Geophys. Res.* **2002**, *107*, 1468. [CrossRef]
33. Curtis, H.D. *Orbital Mechanics for Engineering Students*; Butterworth-Heinemann: Oxford, UK, 2019.
34. Doornbos, E.; Klinkrad, H. Modelling of space weather effects on satellite drag. *Adv. Space Res.* **2006**, *37*, 1229–1239. [CrossRef]